Electronic Supplementary Information (ESI)

Propagation of binarization errors to microstructural parameter uncertainties in X-ray tomographic data of commercial negative lithium ion battery electrodes

P. Pietsch[1], M. Ebner[1], F. Marone[2], M. Stampanoni[2,3] and V. Wood[1*]

[1]*Laboratory for Nanoelectronics, ETH Zuerich, Zuerich, Switzerland*

[2] *Swiss Light Source, Paul Scherrer Institute, Villigen, Switzerland*

[3] *Institute for Biomedical Engineering, University and ETH Zuerich, Zuerich, Switzerland*

1. Experimental and computational methods

Extraction of graphite negative electrodes from commercial cells

Electrodes are extracted from commercial 18650 cells (Samsung 25R6, Samsung E35, Sony VTC5, one cell extracted from a Tesla Model S battery pack) by the following procedure: first, the cells are discharged at a rate of 1C to 0V and held there for 2h. Cells are opened under argon atmosphere before the electrode samples are extracted. The samples are then washed in dimethyl carbonate (DMC), dried, and removed from the glovebox. The Liatrion and Nanotek electrodes were used as shipped.

Tomographic imaging and reconstruction

Tomographic imaging was conducted at the TOMCAT beamline at the Swiss Light Source at an X-ray beam energy of 13 keV. Using the 40x microscope and an sCMOS camera with 2560 x 1200 pixels readout resulted in a pixel size of 162.5 x 162.5 nm^2 and a corresponding field of view of $416 \times 195\ \mu m^2$. For each tomographic scan, 1201 projections at an exposure time of 600 ms were acquired, filtered using the Paganin phase retrieval algorithm[1] ($\delta = 2 \times$

10^{-8}, $\beta = 1 \times 10^{-9}$, $d = 5$ mm), and reconstructed using Fourier-based reconstruction algorithms implemented at the TOMCAT beamline[2].

Histogram processing and calculating the threshold range

Each reconstructed dataset was cropped to a size of 350 x 350 x 150 vox^3 (57 x 57 x 24 μm^3) and linearly rescaled such that 99.98 % of all gray values fall in the [0, 1] interval. The 0.02 % of all voxels with gray values outside the [0, 1] range were neglected for binning the datasets into histograms with 1000 bins.

The eleven different automatic thresholding techniques were applied to the resulting histograms: Otsu[3], Huang[4], Isodata[5], Peak-average (where threshold is defined as the mean of the two peak positions, when the histogram data is fitted with a set of two Gaussians), Minerror[6], Moments[7], Max-Entropy[8], Triangle[9], Yen[10], Shanbhag[11] and Li[12]. They were implemented in MATLAB based on the threshold criteria derived in the respective publications. However, to avoid convergence problems with some iterative methods, all possible thresholds in the [0, 1] histogram range were tested against the respective criteria for each method to find the optimal thresholds.

The mean of the eleven threshold values plus/minus one standard deviation was taken to be the threshold range.

Binarization with the max-flow-min-cut algorithm

Formally, the idea of including morphological information in the segmentation process can be implemented using graph cuts theory[13]. For binarizing our datasets, we used a MATLAB based implementation of the max-flow-min-cut algorithm by Jing Yuan[14–16] available on MATLAB Central[17].

The idea of the max-flow-min-cut algorithm is presented in Figure S1. Each pixel of the image (or in 3D equivalently each voxel) is connected with its neighbors and additionally to

two terminals called ‘source’ (red ball) and ‘drain’ (blue ball). The task of binarizing an image is equivalent to finding the ‘minimal’ cut (orange lines) through the network, which completely separates source from drain. Pixels remaining connected to the source are associated with the foreground and those remaining connected to the drain are associated with the background. The cut is called ‘minimal’, because it is found by minimizing the total cutting cost, which is the sum of costs that we associate with cutting the required connections to separate source from drain (orange lines). The cost associated with cutting an individual connection can be defined to depend on the type of connection (pixel – terminal or pixel – pixel) and the gray value of the respective pixel. For example, if we define the cost of cutting a pixel – source connection as $E_{p-S} = |\mu_p - \mu_D|$, the cost of cutting a pixel – drain connection as $E_{p-D} = |\mu_p - \mu_S|$ (μ_p being the gray value of the respective pixel and μ_S, μ_D being two reference gray values for the source (foreground gray value) and drain (background gray value) terminals respectively) and set the cost for cutting a pixel – pixel connection E_{pp} to zero, a binarization is obtained that is equivalent to thresholding at a level $\frac{\mu_S+\mu_D}{2}$. However, if E_{pp} is finite, pixels can be flipped and assigned to the same phase as their neighboring pixels (see Fig. 2 in the main text). The higher E_{pp} is compared to E_{p-S} and E_{p-D}, the more expensive it will be to associate neighboring voxels with different domains. We therefore define E_{pp} as the filtering parameter for the binarization process, which controls feature preservation and smoothness of the binarization (“alpha” parameter in the MATLAB code[17]). A rigorous mathematical treatment and background information on graph cuts theory and max-flow-min-cut algorithms can be found in references[13–16].

We chose the two terminal reference values μ_S and μ_P symmetrically above and below a given threshold. The binarization process is then entirely defined by the two input parameters (i) threshold and (ii) cost for cutting a pixel – pixel connection E_{pp}.

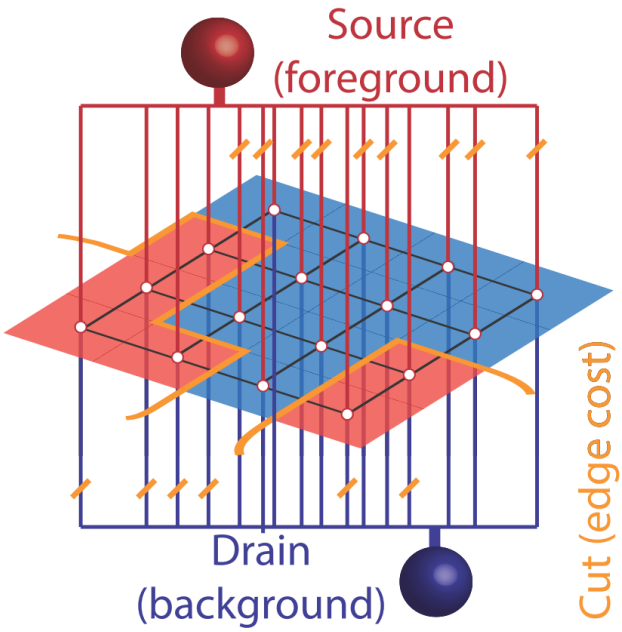

Figure S1. Illustration of the max-flow-min-cut principle

Microstructure calculations

All microstructure characteristics were calculated on the binarized data as obtained from the max-flow-min-cut algorithm, using MATLAB based custom implementations. The definition of the tortuosity is based on[18]; the resulting linear system of equations is assembled based on[19] and solved with the MATLAB pre-implemented conjugate gradients squared method. For the specific surface area calculation, the surface was represented using triangulation and divided by the corresponding active material volume, which was calculated from Gauss' divergence law.

2. Gravimetric measurements of electrode porosities

The focus of this work is to quantify the binarization uncertainty of X-ray tomographic data, as well as the resulting uncertainty in the microstructural parameters. However, measuring porosities, tortuosities, or specific surface areas with different experimental techniques (e.g. mercury intrusion, X-ray tomography, gravimentric measurements, electrochemical impedance spectroscopy, BET, etc…) can help in understanding limitations to different methods and subtle differences among them. The results may greatly differ from one another and these variations reflect the differences in what the technique is probing.

For example, porosity of an electrode can be determined from a combination of gravimetric, thickness, and helium pycnometry measurements: (i) From thickness and gravimetric measurements of both the current collector alone and the entire electrode sheet, the volumetric loading (ρ_{vl}) of the coating can be determined. (ii) From the helium pycnometry measurements, the effective density (ρ_{eff}) of the solid phase can be obtained (weighted density of the active material, carbon black, binder, and potential other additives). We have conducted these measurements for three of the seven electrodes:

	ρ_{vl} - volumetric loading (g/ml)	ρ_{eff} - eff. bulk density (g/ml)
25R6	1.46 ± 0.08	2.21 ± 0.03
E35	1.39 ± 0.03	2.17 ± 0.03
VTC5	1.43 ± 0.07	2.22 ± 0.03

The indicated standard deviations are calculated from measuring several samples from each electrode. The porosity can then be calculated according to: $\epsilon = \frac{V_{\mathrm{pore}}}{V\mathrm{total}} = 1 - \frac{V_{\mathrm{solid}}}{V\mathrm{total}} = 1 - \frac{\rho_{\mathrm{vl}}}{\rho_{\mathrm{eff}}}$, which leads to the results shown in Figure S42:

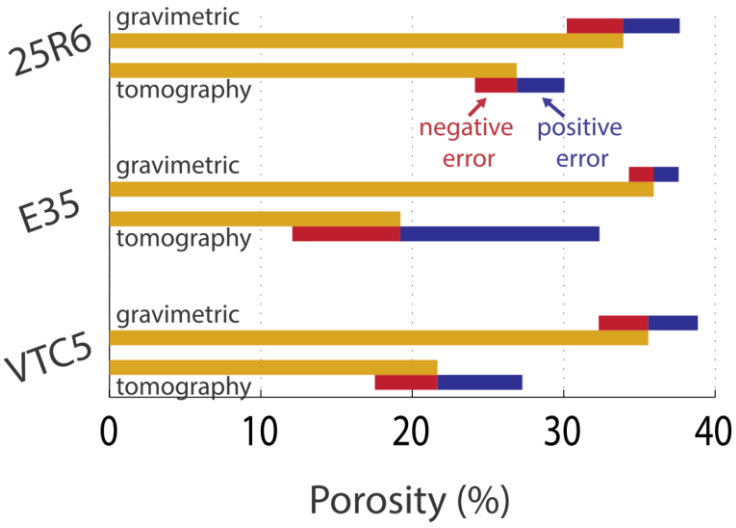

Figure S2. Comparison of porosities obtained from the tomographic and the gravimetric measurements.

The porosities from the gravimetric measurements are always higher than the porosities determined through tomography. This systematic deviation likely stems from the porosity contribution of many tiny pores and substructures within the active material particles that are (partially) below the spatial resolution limit of microtomography. In other words, the active material does not only consist of dense particles with a uniform bulk density equal to the one of graphite.

To illustrate this potential explanation, Figure S43 (top part) shows binarizations of the Sony VTC5 electrode data (i) with the target porosity obtained from the tomographic analysis as presented in the main text (22 %) and (ii) with the target porosity obtained from the gravimetric experiments (36 % porosity).

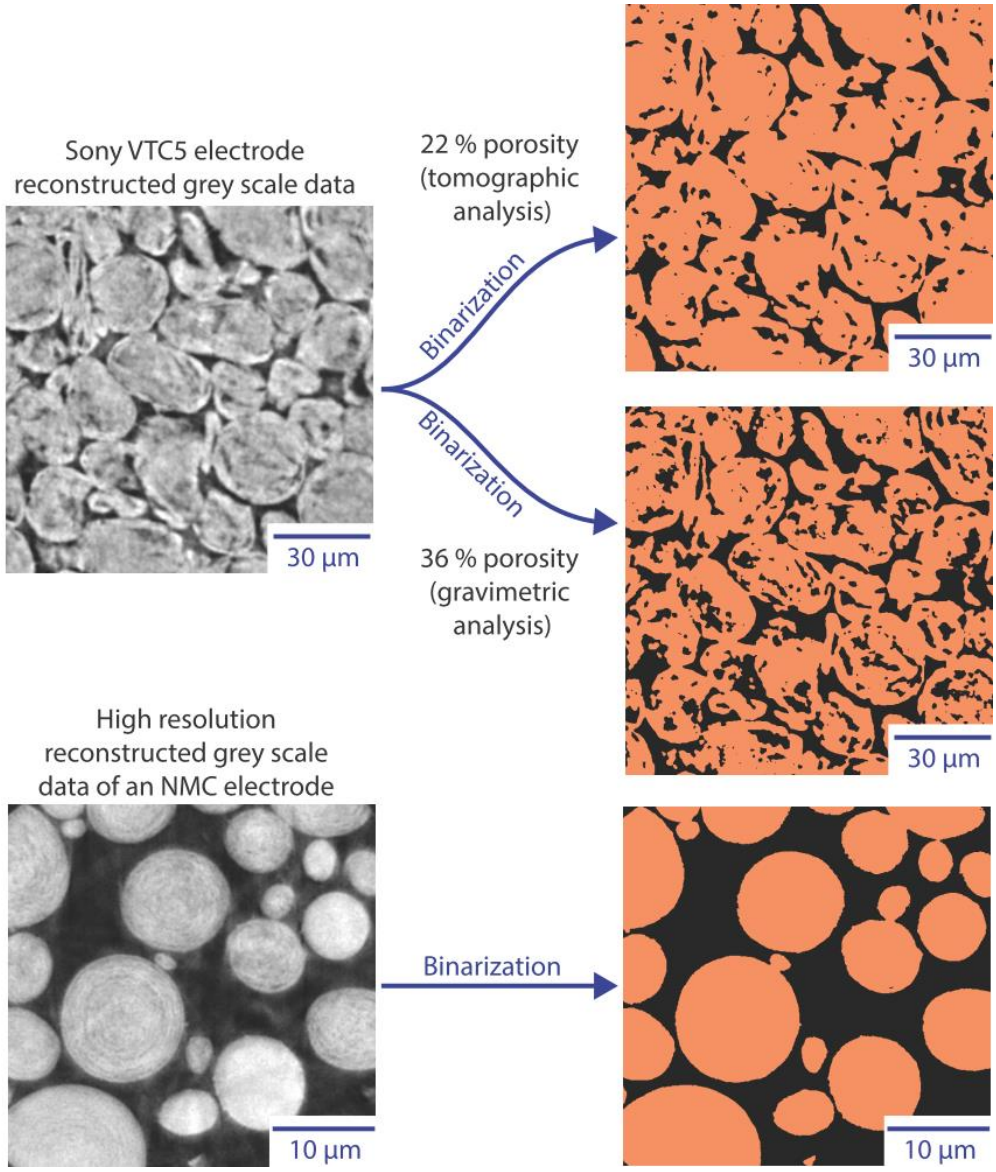

Figure S3. Top: comparison of the binarizations resulting from the tomographic analysis (22 %) and the gravimetric analysis (36 %). Bottom: binarization of an NMC cathode.

As evident from the images, the inhomogeneous gray value distributions within the active particles allows for different binarization interpretations. While the binarization with 36 % porosity matches the target porosity obtained from the gravimetric measurements, it is not necessarily be the better choice for microstructure analysis: the non-enclosed pores between the particles are likely overestimated to compensate for the tiny (enclosed) pores within the active material that are below the spatial resolution limit of the tomography. Because only non-enclosed pores in a microstructure are relevant for its transport properties, an

overestimation of pore space using gravimetric approach could result in large errors in transport measurements.

In Figure S43 (bottom part), we show that this interpretation ambiguity does not occur for electrodes consisting of dense cathode materials of uniform density. In this case, binarization is very reliable and the porosity estimates from the known material composition of the electrode may be exploited to constrain the binarization protocol[20].

The above presented analysis illustrates (i) that comparing different measurement techniques can be difficult, because different constraints are attached to each technique, and (ii) that a very precise definition of the quantity (e.g. all pores space between particles and within particles) to be measured is required.

3. Validation of microstructural uncertainties in anodes with additional cathode data

To validate the idea that high Otsu interclass variances correlate with low microstructural uncertainties also for different sample materials or imaging conditions, Figure S4 expands our analysis on two commercial LIB cathodes. Both samples show very small microstructure uncertainties at large Otsu interclass variances in agreement with our findings on graphite-based electrodes.

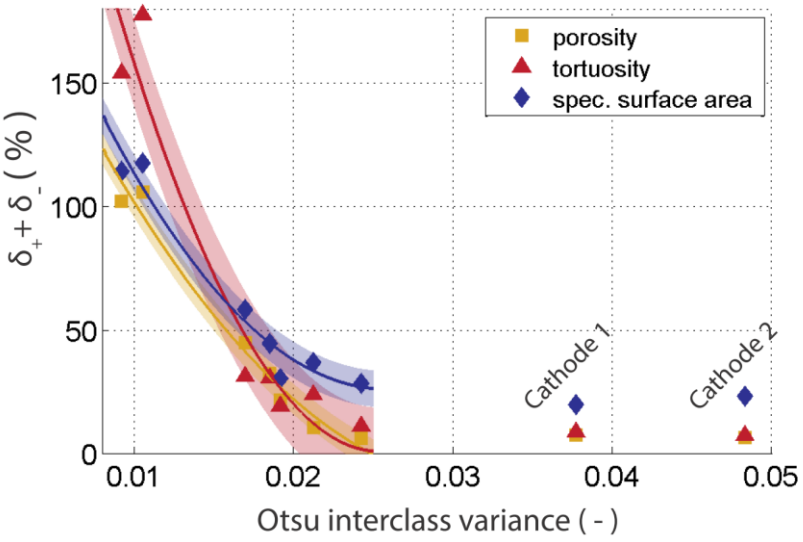

Figure S4. Validating data from two cathodes.

4. Detailed evaluation of all electrodes

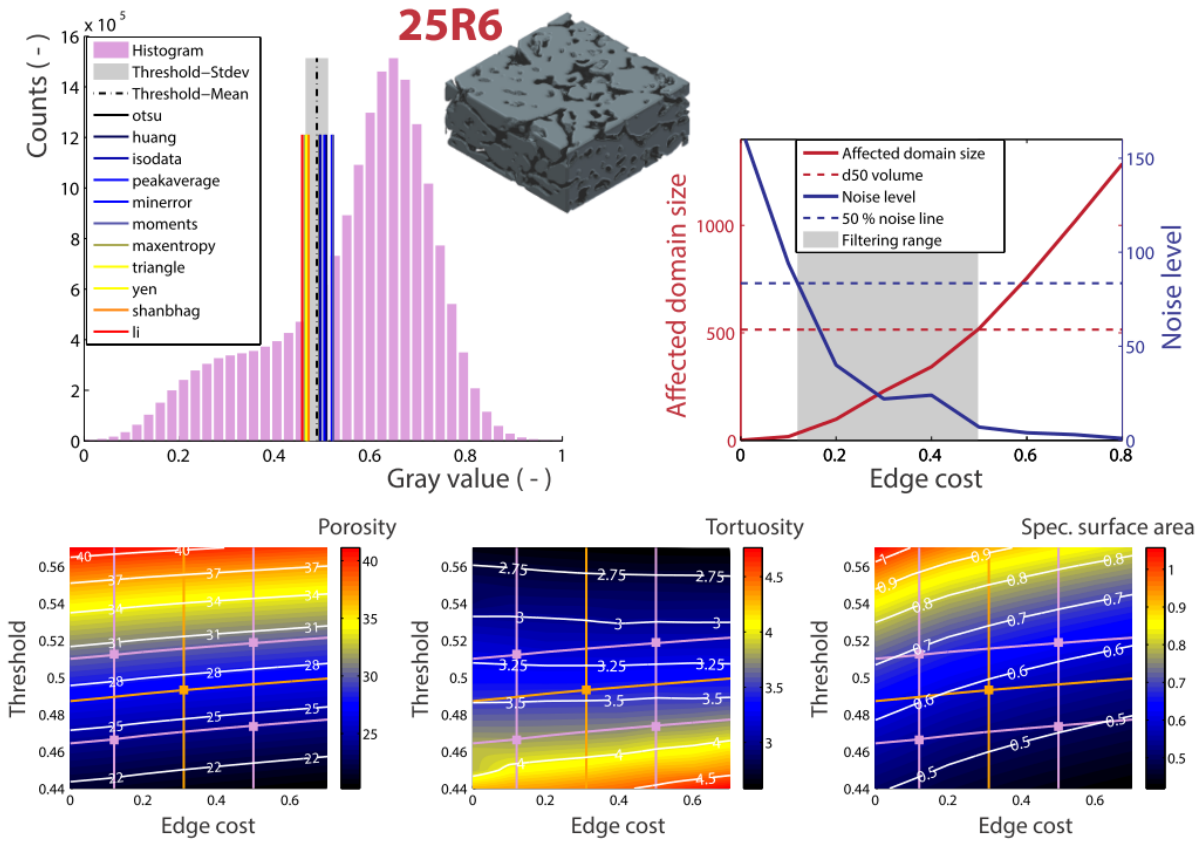

Figure S5. Uncertainty analysis of the Samsung 25R6 electrode.

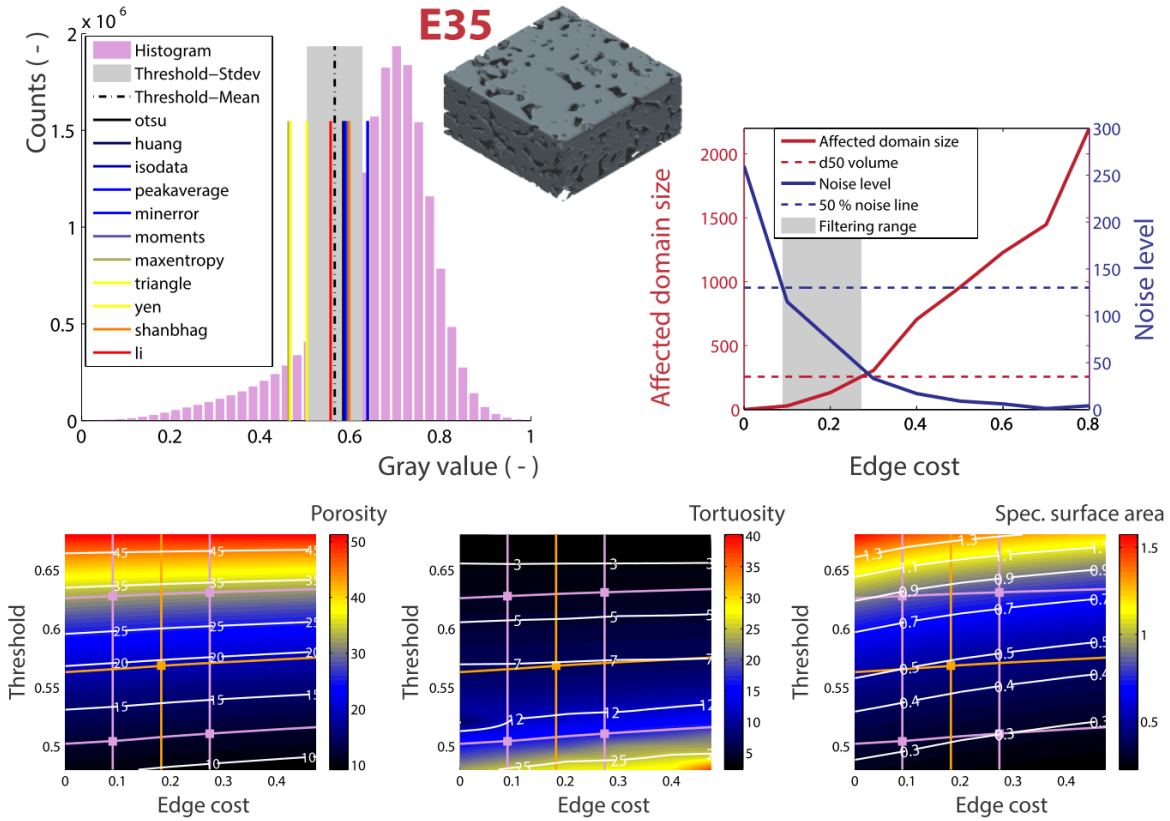

Figure S6. Uncertainty analysis of the Samsung E35 electrode.

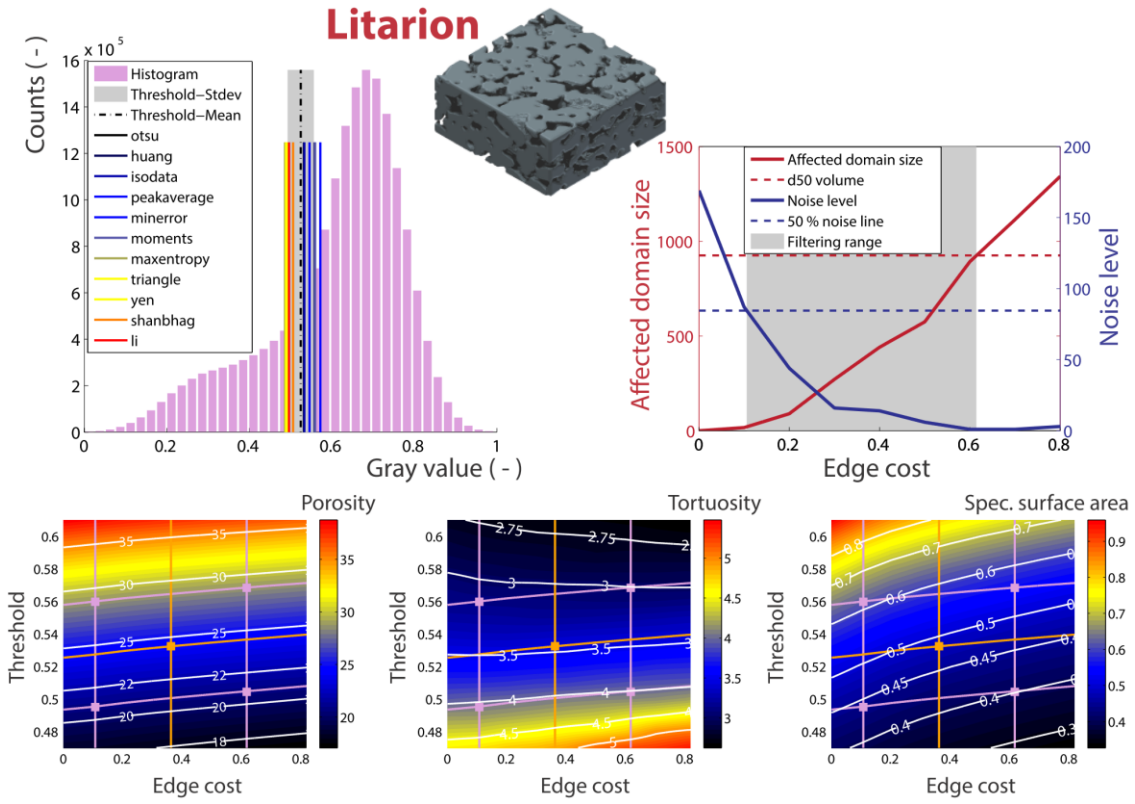

Figure S7. Uncertainty analysis of the Litarion electrode.

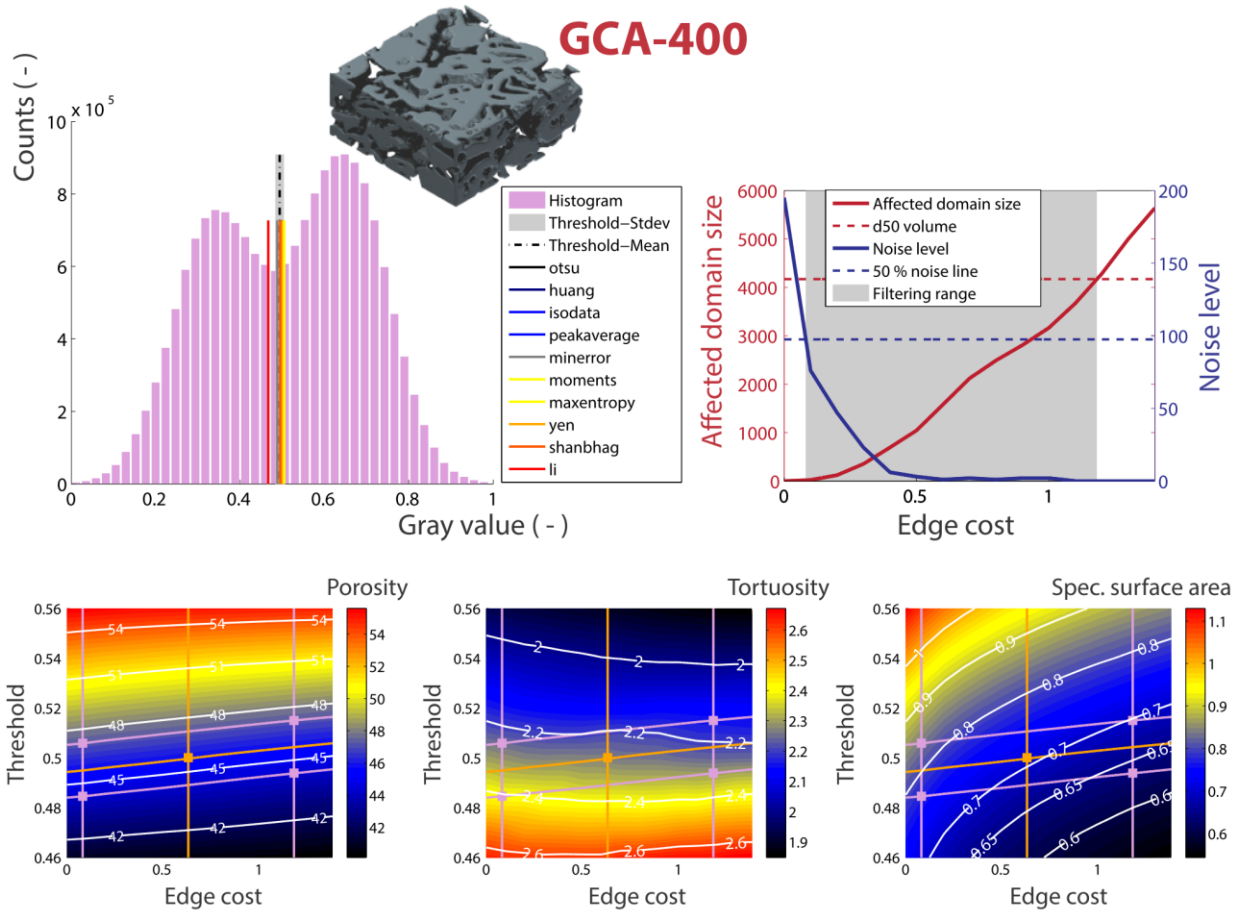

Figure S8. Uncertainty analysis of the Nanotek GCA-400 electrode.

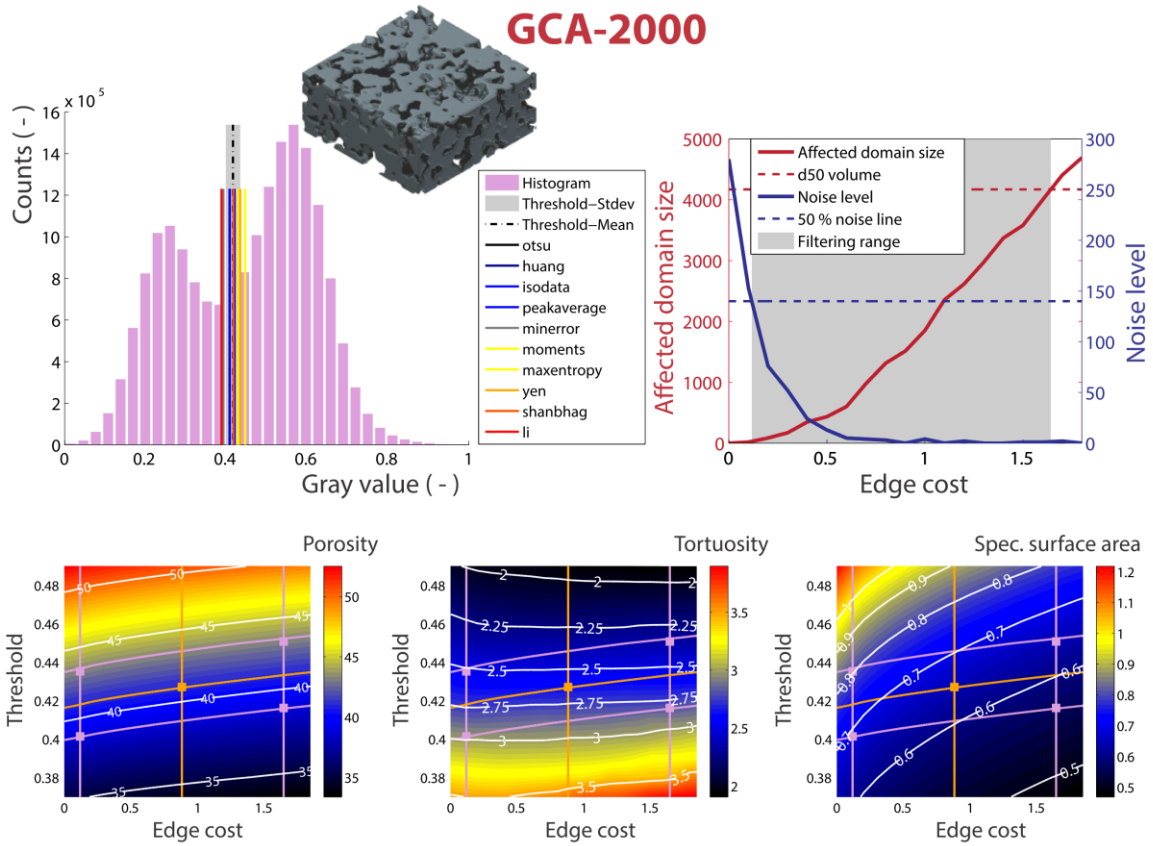

Figure S9. Uncertainty analysis of the Nanotek GCA-2000 electrode.

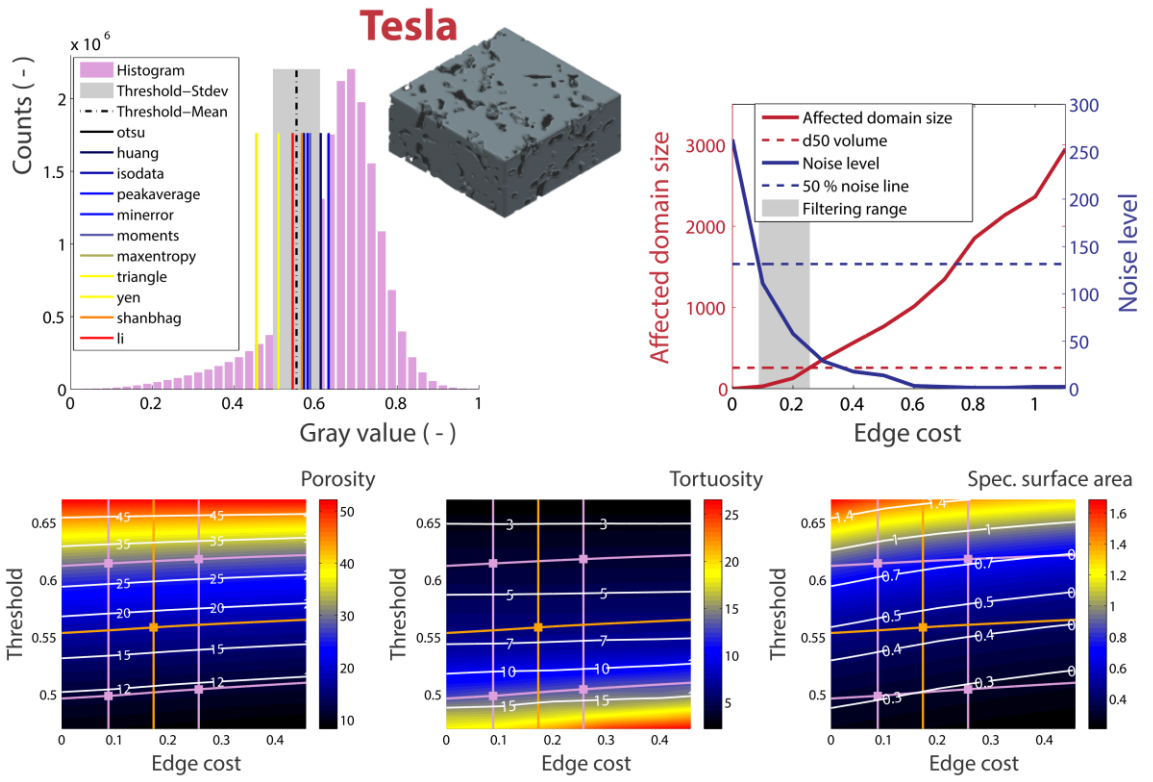

Figure S10. Uncertainty analysis of the Tesla electrode.

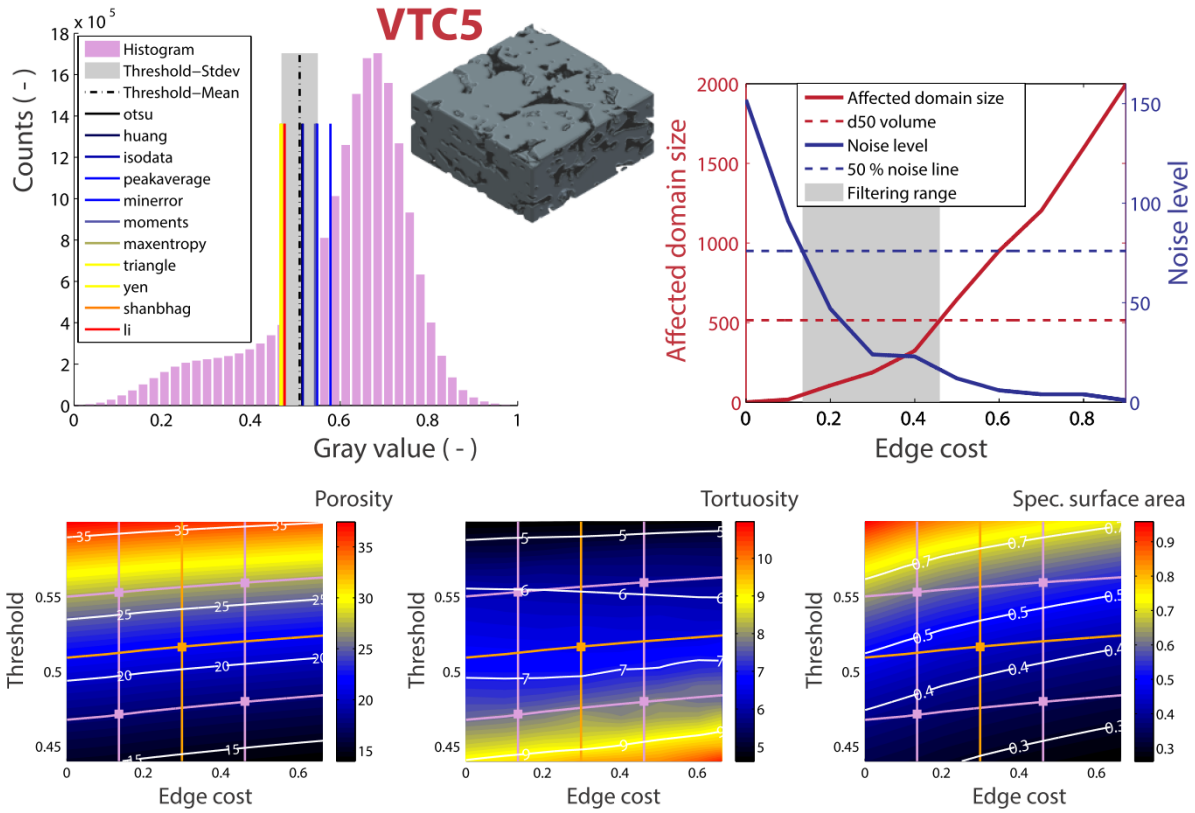

Figure S11. Uncertainty analysis of the Sony VTC5 electrode.

4. Supplementary References

1 D. Paganin, S. C. Mayo, T. E. Gureyev, P. R. Miller and S. W. Wilkins, *J. Microsc.*, 2002, **206**, 33–40.

2 F. Marone and M. Stampanoni, *J. Synchrotron Radiat.*, 2012, **19**, 1029–1037.

3 N. Otsu, *IEEE Trans. Syst. Man. Cybern.*, 1979, **9**, 62–66.

4 L.-K. Huang and M.-J. J. Wang, *Pattern Recognit.*, 1995, **28**, 41–51.

5 F. R. Dias Velasco, *IEEE Trans. Syst. Man. Cybern.*, 1980, **10**, 771–774.

6 J. Kittler and J. Illingworth, *Pattern Recognit.*, 1986, **19**, 41–47.

7 W.-H. Tsai, *Comput. Vision, Graph. Image Process.*, 1985, **29**, 377–393.

8 J. N. Kapur, P. K. Sahoo and A. K. C. Wong, *Comput. Vision, Graph. Image Process.*, 1985, **29**, 273–285.

9 G. W. Zack, W. E. Rogers and S. A. Latt, *J. Histochem. Cytochem.*, 1977, **25**, 741–753.

10 Jui-Cheng Yen, Fu-Juay Chang and Shyang Chang, *IEEE Trans. Image Process.*, 1995, **4**, 370–378.

11 A. G. Shanbhag, *CVGIP Graph. Model. Image Process.*, 1994, **56**, 414–419.

12 C. H. Li and C. K. Lee, *Pattern Recognit.*, 1993, **26**, 617–625.

13 D. Greig, B. Porteous and A. Seheult, *J. R. Stat. Soc.*, 1989, **51**, 271–279.

14 J. Yuan, E. Bae, X.-C. Tai and Y. Boykov, in *Computer Vision - Eccv 2010, Pt Vi*, 2010, vol. 6316, pp. 379–392.

15 J. Yuan, E. Bae, X.-C. Tai and Y. Boykov, *2010 IEEE Conf.*, 2010, **7**, 2217–2224.

16 J. Yuan, C. Schörr and G. Steidl, *SIAM J. Sci. Comput.*, 2007, **29**, 2283–2304.

17 J. Yuan, Fast continuous max-flow algorithm to 2D/3D image segmentation, https://ch.mathworks.com/matlabcentral/fileexchange/34126-fast-continuous-max-flow-algorithm-to-2d-3d-image-segmentation?focused=5205614&tab=function, (accessed 10 July 2017).

18 D. Kehrwald, P. R. Shearing, N. P. Brandon, P. K. Sinha and S. J. Harris, *J. Electrochem. Soc.*, 2011, **158**, A1393.

19 M. Ebner, ETH Zürich, 2014.

20 M. Ebner, F. Geldmacher, F. Marone, M. Stampanoni and V. Wood, *Adv. Energy Mater.*, 2013, **3**, 845–850.